Chemical Engineering Journal 523 (2025) 166453

Contents lists available at ScienceDirect

Chemical Engineering Journal

journal homepage: www.elsevier.com/locate/cej

Revisiting *De Magnete*: Printed routes for tunable magnetoelectricity in energy-efficient devices

R. Carvalho [a], L. Amorim [a], C. Ribeiro [a], S. Lanceros-Mendez [a,b,c,*], M. Serpelloni [e], G. Polidori [e], P. Martins [a,d,*]

[a] Physics Centre of Minho and Porto Universities (CF-UM-UP) and LaPMET - Laboratory of Physics for Materials and Emergent Technologies, University of Minho, 4710-057, Braga, Portugal
[b] BCMaterials, Basque Center for Materials, Applications and Nanostructures, UPV/EHU Science Park, 48940, Leioa, Spain
[c] IKERBASQUE, Basque Foundation for Science, 48009, Bilbao, Spain
[d] IB-S Institute of Science and Innovation for Sustainability, University of Minho, 4710-057, Braga, Portugal
[e] Department of Information Engineering, University of Brescia, Via Branze 38, 25123, Brescia, Italy

ARTICLE INFO

Keywords:
Magnetoelectric composites
Printed electrode engineering
Spintronics
Flexible functional materials
Chemical engineering of interfaces

ABSTRACT

Magnetoelectric (ME) composites are emerging as key functional materials for sustainable and low-power spintronic systems. In this work, we investigate the role of printed electrode thickness in modulating the direct and converse ME responses of flexible P(VDF-TrFE)-based nanocomposites with magnetostrictive fillers. By implementing a scalable fabrication strategy combining Aerosol Jet Printing and photonic sintering, we achieved a 270 % increase in the generated magnetic field (up to 34 Oe) and an 80 % enhancement in the converse ME coefficient, reaching values above 9 mOe·cm·V^{-1}. These values surpass, by more than two orders of magnitude, the electric-field threshold required for spin manipulation, underscoring the relevance of this approach for energy-efficient spintronic operation.

In particular, the maximum magnetic field was generated under 20 V with nanowatt-level power consumption, representing a reduction of up to 6 orders of magnitude compared to current-driven field generation methods.

The printed electrode structuring improves interfacial charge distribution while preserving the composite's mechanical integrity and piezoelectric activity. This study demonstrates how principles rooted in De Magnete can be translated into modern engineering strategies for the development of tunable, high-performance ME devices, contributing to the advancement of sustainable electronics and next-generation energy systems.

1. Introduction

The study of magnetism, from ancient observations to modern electrodynamics, has shaped our understanding of field–matter interactions. Notably, William Gilbert's *De Magnete* laid the foundation for structured magnetic control: an idea that remains relevant in the design of magnetoelectric materials today [1]. The 19th century ushered in revolutionary discoveries that shaped our modern understanding of electromagnetism [2]. In 1820, Hans Christian Ørsted uncovered the relationship between electricity and magnetism, demonstrating that an electric current could influence a magnetic needle [3]. This was followed by Michael Faraday's discovery of electromagnetic induction in 1831, laying the groundwork for electric motors and generators [4]. James Clerk Maxwell then unified electricity and magnetism in his electromagnetic theory in 1865, paving the way for numerous energy generation, communication and data storage applications [5]. This progression, from foundational magnetic theory to functional materials design, mirrors the shift in modern chemical engineering toward the development of tailored material systems for scalable device integration and energy-efficient operation [6,7].

Building upon this rich legacy, the emergence of magnetoelectric (ME) materials represents a transformative leap forward, allowing the direct control of magnetism through electric fields and vice versa [8–10]. This capability paves the way for transformative applications in sensors, actuators, energy harvesters, and spintronic devices [11–14].

Polymer-based ME materials, particularly those combining

* Corresponding authors at: Physics Centre of Minho and Porto Universities (CF-UM-UP) and LaPMET - Laboratory of Physics for Materials and Emergent Technologies, University of Minho, 4710-057, Braga, Portugal.
E-mail addresses: senentxu.lanceros@bcmaterials.net (S. Lanceros-Mendez), pmartins@fisica.uminho.pt (P. Martins).

https://doi.org/10.1016/j.cej.2025.166453
Received 16 April 2025; Received in revised form 17 July 2025; Accepted 24 July 2025
Available online 3 September 2025

piezoelectric polymers such as P(VDF-TrFE) with magnetostrictive additives, offer distinct advantages over single-phase and ceramic-based ME materials [9,15–17]. Unlike single-phase ME materials, which typically exhibit weak coupling, and ceramics, which are brittle and dense; polymer-based materials are lightweight, flexible, and mechanically robust [18–20]. These attributes make them suitable for applications requiring mechanical adaptability, such as wearable devices and flexible electronics [9,21].

Beyond polymer-based nanocomposites, other architectures, such as multiferroic heterostructures, layered laminates, and origami/kirigami-inspired structures, have also demonstrated significant ME performance [22–24]. Comparative analysis of these systems highlights the unique advantages of polymer-based nanocomposites, particularly in terms of flexibility, tunability, ease of processing and compatibility with scalable manufacturing methods, including printing [25].

Such ME nanocomposites offer a unique advantage in spintronic applications, where efficient and precise control of magnetic states is essential for advanced data storage, logic, and sensing technologies [8]. Although 0–3 ME composites typically exhibit lower ME coupling coefficients than 2–2 or 1–1 laminate architectures, they offer distinct advantages for spintronic integration. Their mechanical flexibility enables deposition on non-planar and deformable substrates, while solution-based processing routes are compatible with scalable, low-temperature fabrication. By enabling an electric-field-driven modulation of magnetization, these materials eliminate the need for bulky external magnetic field generators, significantly reducing power consumption [26]. Their tunable properties, mechanical flexibility, and high ME coupling make them particularly suited for next-generation spintronic devices that demand miniaturization and energy efficiency [8,16,26]. More than just functional materials, ME nanocomposites represent a paradigm shift in spintronic engineering, offering an environmentally sustainable alternative that aligns with the increasing need for low-power, high-performance electronics [8,27,28]. However, fully exploiting the potential of these materials requires precise engineering of the electrode architecture, as the efficiency of ME coupling is strongly dependent on the electrode's thickness, material properties, and integration with the composite, with respect to the interface characteristics [29]. Optimizing the electrode design is therefore crucial to enhancing the ME response, ensuring efficient energy transfer and unlocking the full capabilities of ME nanocomposites in spintronic devices [29]. Additionally, the proper electrode thickness enhances device stability, longevity, and energy efficiency, while playing a fundamental role in governing charge distribution, mechanical stability, and interfacial interactions in ME composites [30–32]. However, a systematic investigation of the influence of printed electrode architecture, particularly thickness, on the ME response of flexible composites remains scarce, despite its critical role in optimizing interfacial coupling and field generation efficiency.

While thinner electrodes allow for higher resonance frequencies, they can compromise mechanical durability and field uniformity.

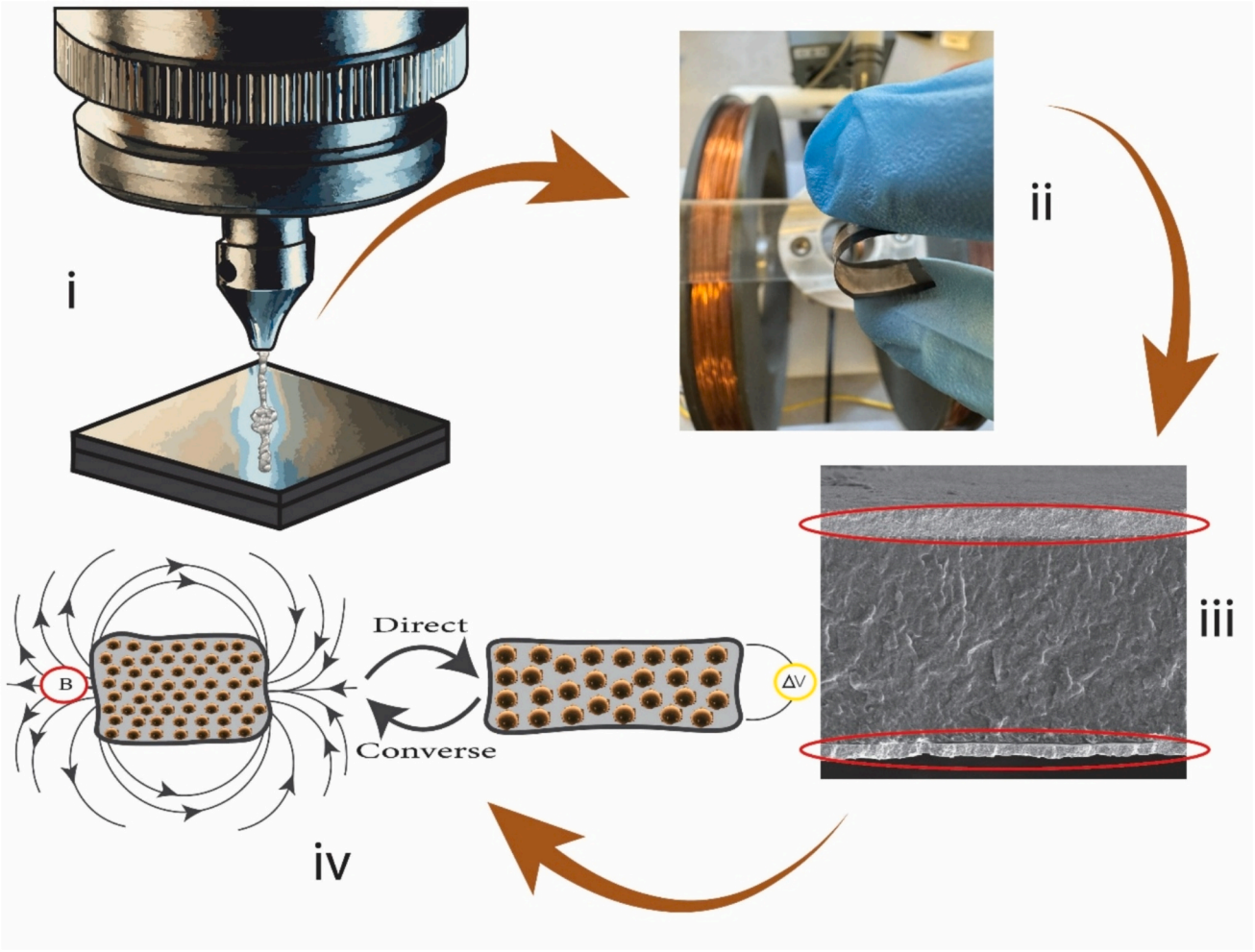

Fig. 1. Representative scheme of the proposed approach. i) Aerosol Jet printing of the thick conductive electrode optimizing charge distribution and interfacial coupling; ii) photograph of the flexible ME sample with jet printed electrodes; iii) SEM image of the ME sample with jet printed electrodes (highlighted with red ellipses); iv) Direct and converse ME effects.

Conversely, thicker electrodes provide greater robustness and optimized mass-loading effects, significantly improving the coupling between the piezoelectric and magnetostrictive phases as a result of the optimization of charge distribution and interfacial coupling [33–35]. Thus, properly tuned electrode thickness maximizes the ME coupling coefficient, making it a key parameter in the design of advanced ME systems not only for spintronic devices but also for sensors, actuators and energy harvesters [36,37] (Fig. 1).

The deposition of thick electrodes on piezoelectric composites, such as P(VDF-TrFE)-based ones, by sputtering or thermal evaporation presents significant challenges due to the extended processing times and elevated energy requirements, which can lead to depolarization of the polymer matrix [38,39]. This depolarization negatively impacts the piezoelectric properties, reducing the overall efficiency and reliability of the ME composite [40]. Additionally, conventional high thermal and mechanical stresses deposition techniques, such as sputtering, electron beam evaporation, and thermal evaporation, may induce structural deformations, compromising the polymer's functional integrity [41,42].

This creates a critical bottleneck in interface design, particularly when aiming to maximize charge distribution, mechanical stability, and long-term performance. Overcoming these limitations requires alternative, low-energy fabrication strategies capable of precisely structuring conductive elements without degrading functional integrity. In this context, Aerosol Jet Printing (AJP) emerges as an advanced and scalable solution, enabling the deposition of thick, patterned electrodes at low processing temperatures, with micrometric precision and excellent material compatibility [43,44]. This non-contact technique not only preserves the structural and functional integrity of piezoelectric polymers, but also introduces new design freedom for interface engineering [44,45]. Its integration into ME composite fabrication represents a smart and versatile strategy bridging the gap between materials science and advanced chemical engineering strategies for sustainable device integration.

Thus, this study systematically investigates the impact of electrode thickness in polymer-based ME composites, analyzing its effects on ME coupling efficiency. We explore a range of magnetostrictive fillers and employ advanced electrode deposition techniques such as photonic curing to overcome conventional fabrication limitations [46]. This approach not only overcomes the challenges of thick electrode fabrication but also enhances the performance and durability of ME systems, making it a promising solution for developing robust and energy-efficient devices.

For this purpose, we incorporated six distinct magnetostrictive fillers (Table 1):

i) $CoFe_2O_4$ nanoparticles, selected for their high saturation magnetization and remarkably high negative magnetostrictive coefficient (−250 ppm), unparalleled among ferromagnetic nanoparticles [47];
ii) Fe_3O_4 nanoparticles recognized for their superparamagnetic nature and high magnetostriction of approximately 50 ppm [8];
iii) $Nd_2Fe_{14}B$ featuring moderate magnetostriction (20 ppm) and elevated magnetic energy product. Its inclusion provides equilibrium to the composite's overall performance by contributing to both magnetostriction and high energy density [8];
iv) $Ni_{80}Fe_{17}Mo_3$ permalloy nanopowder with a magnetostriction of 160 ppm [48]. This material offers powerful magnetoelastic effects, enhancing the composite's overall sensitivity and improving performance under lower magnetic field conditions.
v) $Ni_{0.5}Zn_{0.5}Fe_2O_4$ with a negative magnetostriction of −8 ppm [49], which provides a unique tuning capability within the composite system. The incorporation of Zn into the spinel ferrite structure increases electrical resistivity while preserving magnetoelastic coupling, thus minimizing eddy current losses and enhancing energy efficiency in ME devices.
vi) $Co_{0.5}Zn_{0.5}Fe_2O_4$ nanopowder with a magnetostriction of 10 ppm. Adding Zn to $CoFe_2O_4$ improves the magnetoelastic response and increases the electrical resistivity resulting from the Zn doping on the A-site of the spinel structure of $CoFe_2O_4$ [50,51].

Table 1
Size and magnetostrictive coefficient (λ) of the magnetic particles used in this study.

Filler	Size (provided by the supplier)	λ (ppm)
$CoFe_2O_4$	35–50 nm	−250
Fe_3O_4	30 nm	50
$Nd_2Fe_{14}B$	5 μm	20
$Ni_{0.5}Zn_{0.5}Fe_2O_4$	10–30 nm	−8
$Ni_{80}Fe_{17}Mo_3$	70	160
$Co_{0.5}Zn_{0.5}Fe_2O_4$	30–50 nm	10

These additives were integrated within P(VDF-TrFE), a polymer renowned for its exceptional piezoelectric properties [52,53] ($|d_{33}| = -38\ pC{\cdot}N^{-1}$ and surpassing all other polymers), chemical and physical stability, and manufacturing versatility, including its suitability for 3D printing techniques [52,54]. This polymer base offers remarkable mechanical pliability, highly suitable for bendable and body-worn sensor applications [52]. Its inherent piezoelectric characteristics also amplify the overall ME interaction within the composite structure [15,55].

2. Materials and methods

2.1. Materials

The foundational component for the nanocomposites, P(VDF-TrFE), was obtained from Piezotech, consisting of 70 mol% vinylidene fluoride and 30 mol% trifluoroethylene. Dimethylformamide (DMF), acquired from Merck, served as the solvent for dissolving the polymer. The magnetic additives integrated into the composite films encompassed $CoFe_2O_4$ nanoparticles, Fe_3O_4 nanoparticles, $Nd_2Fe_{14}B$ micropowder, $Ni_{0.5}Zn_{0.5}Fe_2O_4$ nanoparticles, $Co_{0.5}Zn_{0.5}Fe_2O_4$ nanopowder, and $Ni_{80}Fe_{17}Mo_3$ nanopowder. All these materials were obtained from Nanostructured & Amorphous Materials Inc. (USA), with the exception of the $Nd_2Fe_{14}B$ micropowder, which was sourced from Magnequench GmbH (Germany). Size and magnetostrictive coefficient (λ) of the magnetic particles used in this study can be found in Table 1.

The selection of the six magnetostrictive fillers used in this study was carefully made to cover a representative range of magnetostriction coefficients, magnetic behaviors (from soft to hard magnetic materials), electrical resistivities, and particle sizes, all of which significantly influence the ME response.

2.2. Composite fabrication

Composite films were prepared by dispersing magnetostrictive additives into 10 mL of DMF under ultrasonic treatment (Fisherbrand FB15056 for 5 h), followed by mechanical stirring for 1 h with P(VDF-TrFE) powder to ensure even distribution. Each ME composite consisted of 20 wt% magnetostrictive filler and 80 wt% P(VDF-TrFE). Composites with three different weight percentages (5, 10, and 20) of $CoFe_2O_4$ were also prepared to examine the effect of varying magnetostrictive nanoparticle content. The resulting mixture was then applied to clean glass substrates using a doctor blade. After the solvent evaporation, the films were heated at 215 °C for 10 min and then cooled at room temperature. Once removed, the films displayed smooth, flexible, and uniform surfaces with a final thickness maintained between 45 and 60 μm.

2.3. Electrode fabrication/deposition

The conductive layer was fabricated using a silver ink, Smart Screen B (S-CS91349, Smart Aero, Genesink, 13106 Rousset Cedex, France)

deposited via Aerosol Jet printing AJ300 (Optomec, Albuquerque). The Aerosol Jet process utilizes aerodynamic focusing to deposit electronic inks onto substrates with high accuracy. The ink is first placed into an atomizer, which generates a dense mist of material-laden droplets ranging from 1 to 5 μm in diameter. The system uses standard CAD data converted into a vector-based tool path to guide a 2D or 3D motion control system. This enables precise ink patterning, with printed features ranging from 10 μm to several millimeters.

Smart Screen B is a sustainable conductive ink based on silver nanoparticles (AgNP) designed for the printed electronics market. It is particularly suitable for sensor manufacturing and applications requiring high conductivity on flexible substrates and high resolution on paper substrates at room-temperature curing temperatures.

The final thickness of the composite films prior to electroding was maintained between 45 and 60 μm, as verified with a micrometer. This consistent thickness, combined with the uniformity of the printed electrode layer, ensures a stable geometry for ME coupling and facilitates direct comparison across all samples.

The inks were printed using a broad deposition head with a 3 mm nozzle, to cover the entire substrate centrally and rectangularly, an adhesive tape was applied to the part not affected by spraying to keep the sample still during printing.

Since the polymers used cannot withstand temperatures above 60 °C, after being coated with ink, the samples are placed in an oven to dry at 50 °C for at least 4 h. The process was performed twice to both front and back sides of the samples.

The samples subsequently are sintered and cured through the photonic sintering by PulseForge (Pulseforge 1300 – Novacentrix, Austin, TX, USA).

After several tests, the best process parameters of PulseForge were optimized: Potential 430 V; Envelope 3000 μs; uPulse 10 μs; Duty Cycle 25 %; Rate 0.3 Hz; and Repeat 15.

This setup also ensures that the temperature does not exceed 60 °C for an extended period. The potential indicates the voltage applied to the flash lamp, which determines the energy of the pulses emitted. Higher voltage corresponds to more intense light and heat generation, which can enhance the sintering or curing process, although, it must be controlled to avoid material degradation. The envelope represents the duration of the entire flash lamp pulse, including the rise and fall times. This determines the total exposure time of the material to light. Shorter envelopes minimize heat spread, while longer envelopes allow more heat transfer into the substrate. Pulse refers to the duration of the single pulse within the envelope that creates extreme but localized thermal gradients. The duty cycle is the percentage of time the lamp is active during each cycle, which contributes to balancing energy delivery and the prevention of overheating. Pulse rate defines the number of pulses per second. This parameter not only controls the rate of energy delivery but also allows heat dissipation between pulses. Repetition represents the number of times the entire pulsing process is repeated. More repetitions allow for cumulative energy delivery, ensuring proper sintering or polymerization and minimizing damage to sensitive regions.

For morphological comparison purposes, conventional gold electrodes were deposited on samples using a commercial Polaron model SC502 sputter coater.

2.4. Characterization of ME composite films

The ME composites cross-sectional morphology and particle dispersion were examined using a Nova NanoSEM 200 scanning electron microscope (SEM). Before analysis, each film sample was immersed in liquid nitrogen for 1 min and then cryogenically fractured to obtain a clean fracture surface. This surface was coated with a thin layer of gold palladium to enhance the quality of SEM inspection.

Differential scanning calorimetry (DSC) was used to thermally characterize the produced ME composites. Measurements were performed using a DSC 6000 PerkinElmer instrument, with a temperature range of 30 to 220 °C, a heating rate of 10 °C.min-1, and a 20 mL.min-1 nitrogen flow. The films crystallinity (χc) was determined from the melting enthalpy (ΔHf) using the following Eq. (1):

$$\chi_c = \frac{\Delta H_f}{m\Delta H_f^*} \times 100\% \quad (1)$$

where ΔH_f^* (91.45 $J.g^{-1}$ [56]) is the melting enthalpy of P(VDF-TrFE) with a crystallinity of 100 %, and m its weight fraction in the composite.

The mechanical properties of the ME films without electrodes were evaluated at room temperature under tensile loading conditions, using a deformation speed rate of 0.5 $mm.min^{-1}$ with an Autograph AG-IS (Shimadzu) testing machine equipped with a 500 N load cell. The Young's modulus (E) of the films was determined from the linear portion (up to 0.1 % strain) of the stress-strain curve using Eq. (2):

$$\sigma = E \times \varepsilon \quad (2)$$

where σ is the stress, and ε is the strain.

The DC volume electrical resistivity (ρ) of the samples was obtained by assessing the room-temperature characteristic I/V curves with a Keithley 6487 picoammeter and voltage and Eq. (3):

$$\rho = R \times \frac{wt}{l} \quad (3)$$

where R is the resistance obtained from the slope of the I/V curve, w and l are the width and length of the electrodes, respectively, and t is the thickness of the film measured by a Digimatic Micrometer MDC-25PX. The characteristic surface DC conductivity (σ_{DC}) of each sample was then determined as the inverse of the resistivity, Eq. (4):

$$\sigma_{DC} = \frac{1}{\rho} \quad (4)$$

The films capacitance (C) and dielectric losses (tanδ) were measured using a QuadTech 1920 instrument, applying 0.5 V over a frequency ranging from 1 Hz to 1 × 10^6 Hz at room temperature. Before measurement, circular electrodes with a 5 mm diameter were deposited on both sides of each film. The real part of the dielectric permittivity (ε') was calculated using the Eq. (5):

$$\varepsilon' = \frac{C\,t}{\varepsilon_0 A} \quad (5)$$

where ε' is the dielectric permittivity, C is the capacitance, ε_0 is the vacuum permittivity constant (8.85 × 10^{-12} $F{\cdot}m^{-1}$), and A is the electrode area.

The piezoelectric coefficient (d_{33}) of each film was assessed at room temperature using a model 8000 d_{33} meter from APC Int. Ltd. Before measurement, each film was poled in a homemade corona chamber. The sample was placed approximately 2 cm from the corona grid and exposed to a 15 kV voltage differential at 120 °C for 1 h. The cooling phase was conducted until room temperature while maintaining the same electric conditions.

The direct ME response of the films was evaluated at room temperature using the dynamic method, as represented in Fig. 2. The α_{33} coefficient was calculated using Eq. (6):

$$\alpha_{33} = \frac{V}{d.H_{AC}} \quad (6)$$

The AC driving magnetic field (with a maximum of 3.98 Oe) was provided by a pair of Helmholtz coils. The external bias field was provided by an electromagnet with a maximum value of 1.2 T. The induced ME voltage (V) in the samples was measured using a Standford Research Lock-in amplifier.

The converse ME effect (α'_{33}) was characterized by applying an AC voltage (20 V peak-to-peak) across the printed electrodes at the resonance frequency of each sample. The resulting magnetic field generated

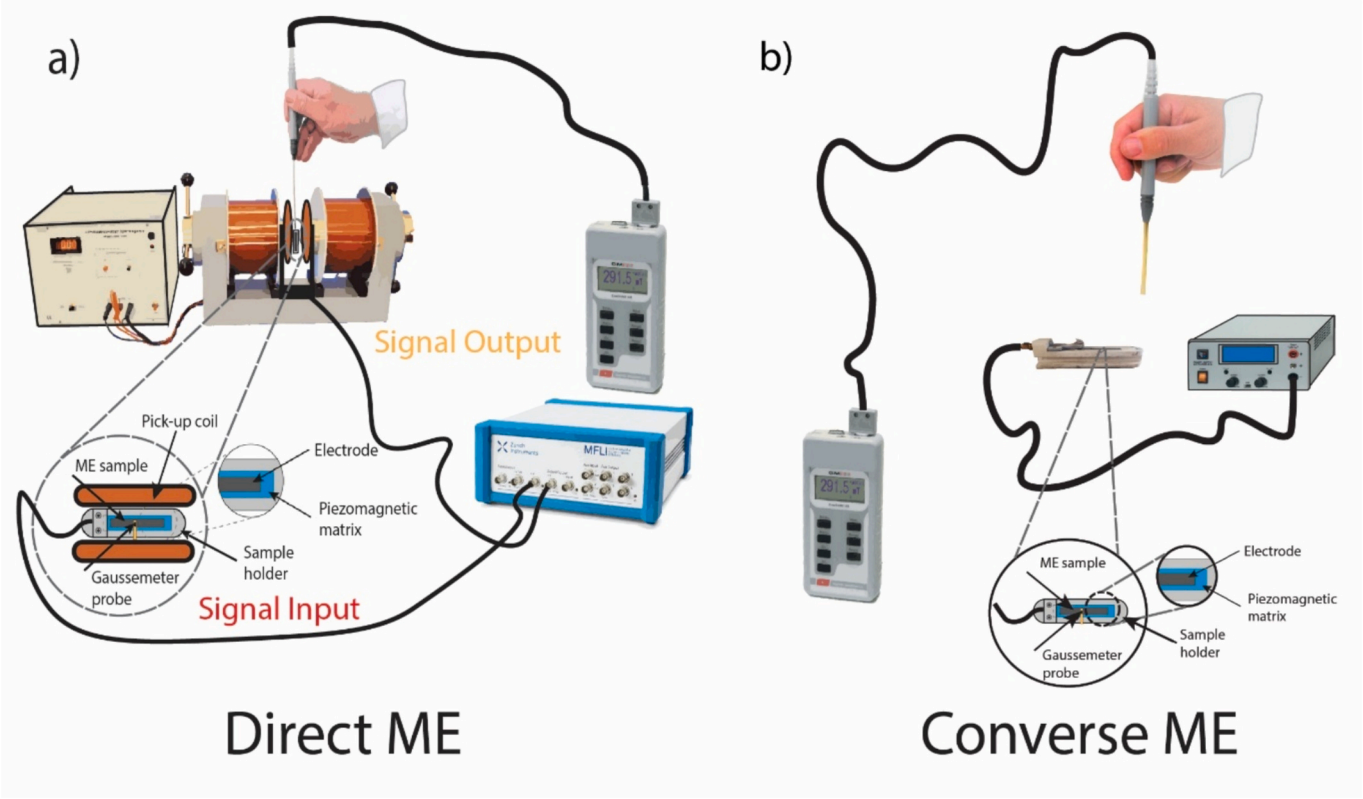

Fig. 2. Representative scheme of ME measurements: a) direct effect; and b) converse effect.

by the sample was measured using Hirst Gaussmeter with PC interface positioned at a fixed distance (~1 mm) from the surface of the composite. The electric field was calculated based on the applied voltage and the measured thickness of the film (~50 μm). The α'_{33} was then determined following the methodology described in [8], using standard CGS-to-SI conversion factors [57], Eq. (7):

$$\alpha'_{33} = \frac{\Delta B}{\Delta E} = \frac{\Delta M \times \rho \times \frac{4\pi}{10000}}{\frac{V}{t}} = \frac{\Delta M \times \rho \times \frac{4\pi}{10000} \times t}{V} \quad (7)$$

where ΔB is the induced magnetic field; ΔE the applied electric field; ΔM the variation of the magnetic saturation between sample under and without applied field; ρ the density of the composite; t the poling distance and V the applied voltage.

2.5. Nomenclature of ME composite films

The subsequent terminology (Table 2) will be employed throughout this document:

Table 2
Designation system for corona-poled ME composites.

Nanoparticle type and wt%	Abbreviation
None	P(VDF-TrFE)
$CoFe_2O_4$; 5	CFO5
$CoFe_2O_4$; 10	CFO10
$CoFe_2O_4$; 20	CFO20
$Co_{0.5}Zn_{0.5}Fe_2O_4$	CZFO20
Fe_3O_4; 20	FO20
$Nd_2Fe_{14}B$; 20	NdFeB20
$Ni_{0.5}Zn_{0.5}Fe_2O_4$; 20	NZFO20
$Ni_{80}Fe_{17}Mo_3$; 20	NFM20

3. Results and discussion

To attain optimal ME coupling, it is essential to comprehend the composites structural, thermal, mechanical, electrical, and magnetic characteristics. Each of these attributes contributes to the efficacy of the ME effect, particularly regarding the interaction between the magnetic and piezoelectric components of the composite.

3.1. Morphological characterization

The morphology of the composite films has a significant impact in ME coupling, since a proper dispersion of magnetostrictive fillers improves their interaction with the piezoelectric polymeric matrix by an effective transfer of mechanical stress. Conversely, a well-bonded and uniform electrode thickness ensures an even electric field over its surface. Therefore, a homogeneous fillers distribution and an optimal electrode deposition are essential to obtain a converse ME effect. Fig. 3 presents the typical cross-section morphology of each composite observed under SEM. Samples with conventional electrodes (vacuum-evaporated on both sides of each sample [8] have been added for comparison).

The cross-sectional SEM images (Fig. 3) clearly distinguish between the two electrodes (left and right columns). The cryogenic fracturing of the samples revealed a typical brittle surface visible in both samples after breakage.

For the conventional electrode (100 nm de Au-P), images (Fig. 3a, c, e, g) few noticeable agglomerations. The adhesion of the electrode to the film is homogeneous and has a thickness of 115 nm.

On the other hand, the images of the printed electrodes (Fig. 3b, d, f, h) show less adhesion in the contact zone with the nanoparticle film. The cryogenic fracture may have caused these little debonding. Importantly, the thickness of the printed electrodes was measured to be approximately 3.71 μm, nearly 300 times thicker than the conventional gold layer. This value corresponds to two sequential layers of silver

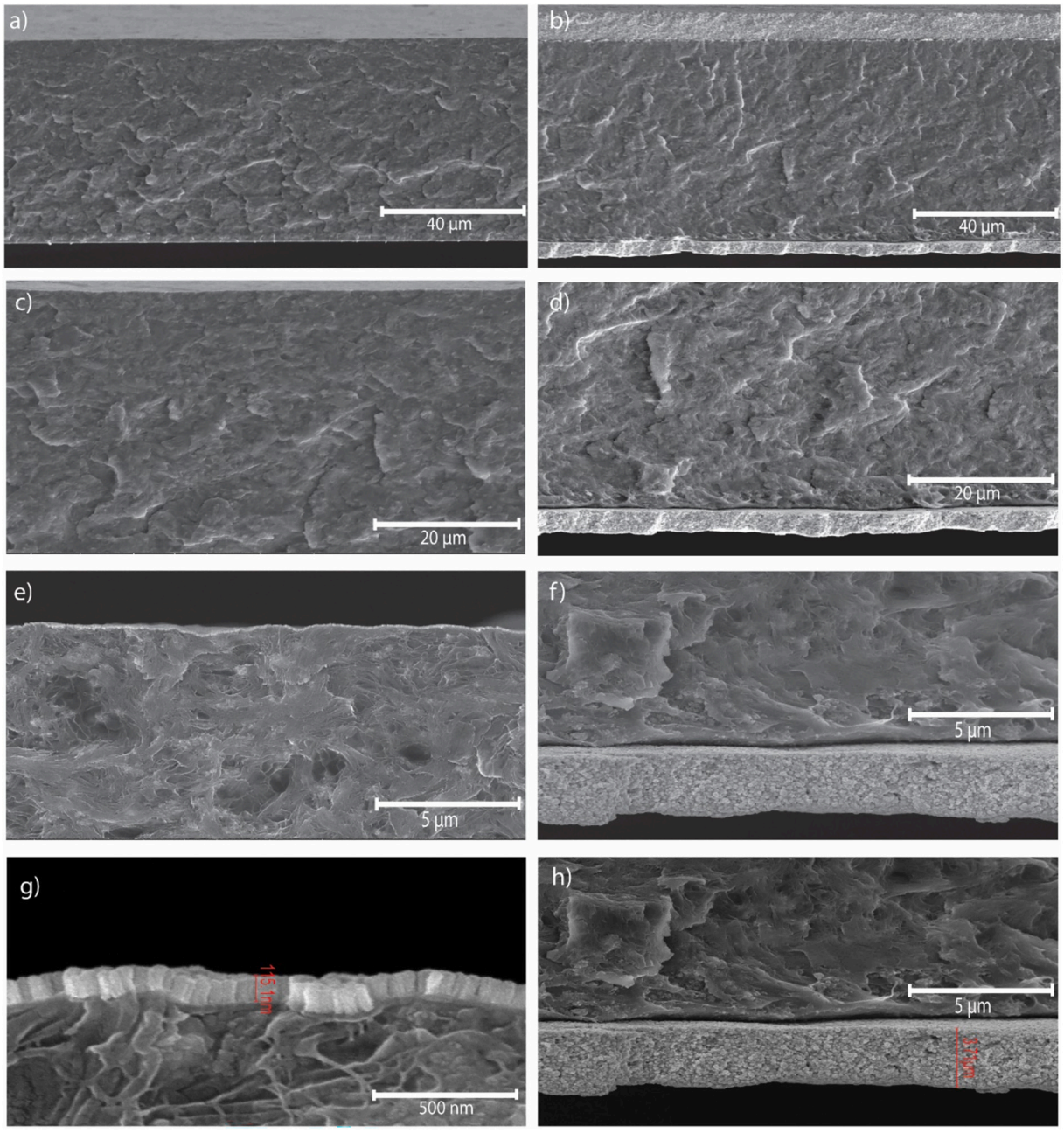

Fig. 3. Cross-section SEM images of CFO 20 composite with conventional electrode (a), c), e), g)) and printed electrodes (b), d), f), h)).

nanoparticle ink deposited via Aerosol Jet Printing and subsequently cured by photonic sintering. This thickness was found to be optimal, enabling superior interfacial coupling and charge distribution. Regarding the ME performance of a nanoparticle film, in particular the converse effect, the greater the thickness and size of the conductive electrode, the better results it will provide [33,35,58]. SEM cross-sections also confirmed good surface homogeneity, with no significant delamination or surface cracking observed post-sintering. The printed electrodes formed a continuous conductive layer with conformal contact, essential for uniform electric field distribution and efficient ME interaction.

3.2. Thermal characterization

The thermal stability and crystallinity of the composites (Fig. 4a and Table 3) are directly related to their ability to maintain structural integrity under operational conditions. High crystallinity and proper thermal transitions ensure that the material can sustain the mechanical strains necessary for ME coupling.

The results revealed that the thermal stability of the composites remained practically unchanged by including magnetic fillers. All samples showed Curie temperature (T_C) at ≈101 °C, while melt temperature (Tm) of the nanocomposites (≈149 °C) showed a slight reduction compared to the P(VDF-TrFE) film (≈151 °C). Crystallinity, however, was found to be sensitive to filler content. Although composites with up to 10 wt% CFO nanoparticles showed no significant change in crystallinity compared to the pure polymer (=27 %), increasing the particle content to 20 wt% caused a notable reduction in crystallinity, ranging from 15 % in CFO20 to 22 % in NFM20. This reduction is consistent with the ability of magnetic particles to act as defects on the crystallization process [59,60].

These crystallization and thermal properties values, such as T_C, Tm

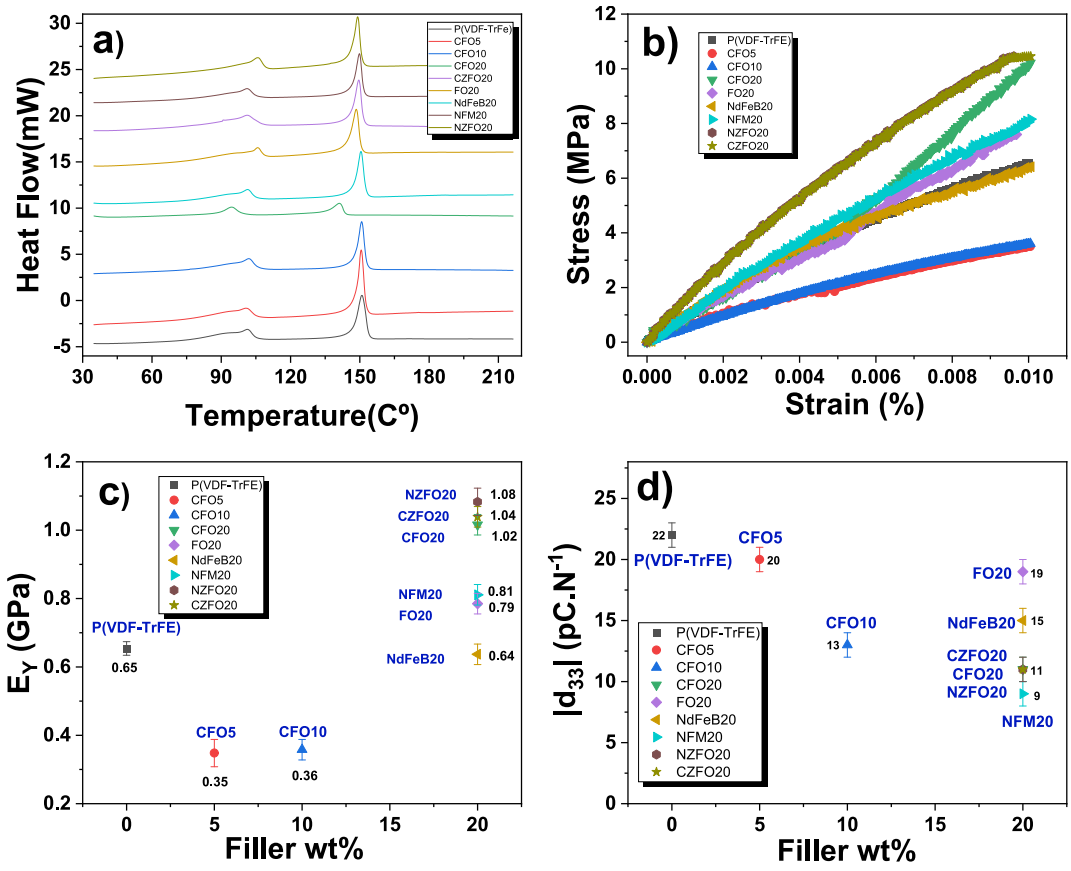

Fig. 4. a) DSC thermogram (heating) for the neat polymer and composites, b) Stress-strain plots for the neat polymer and composites, c) Young's modulus obtained from b) as a function of the filler type and content; and d) $|d_{33}|$ piezoelectric constant as a function of the filler type and content.

Table 3
Curie (T_C) and melt (T_m) temperatures, melting enthalpy (ΔH_f) and crystallinity percentage (χ_c), determined under DSC, for the neat polymer and composites.

Sample	T_C (±0.2 °C)	T_m (±0.2 °C)	ΔH_f ((±1 J/g)	χ_c (±1 %)
P(VDF-TrFE)	101.3	150.9	25	27
CFO5	100.7	150.5	25	26
CFO10	102.0	150.8	19	26
CFO20	94.5	141.2	11	15
FO20	105.8	148.4	22	20
Nd20	101.4	150.4	21	19
NFM20	101.2	149.8	16	22
NZFO20	105.8	149.1	20	17
CZFO20	101.3	149.6	17	16

and fusion enthalpy (ΔH_f) align with expectations since, as they increase, more energy is needed to break down the well-ordered crystalline regions during heating [61,62].

3.3. Mechanical properties

Mechanical properties, namely tensile strength and Young's modulus (E_Y), are critical for effective ME coupling. These properties determine the material's ability to transfer deformation between the piezoelectric and magnetostrictive phases (Fig. 4b–c).

The stress-strain curves (Fig. 4b) revealed a predominantly elastic deformation of all films up to 0.01 strain. Notably, the CZFO20 and NZFO20 samples demonstrate the highest load-baring capability at this strain value, followed by CFO20, NdFeB20, NFM20, FO20, neat P(VDF-TrFE) film, and finally, CFO10, and CFO5 composites. The Young's modulus of each sample was determined at the linear stage of the curve using Eq. (2). The inclusion of CFO nanoparticles up to 10 wt% and 20 wt% NdFeB microparticles led to a reduction in E_Y (0.35–0.64 GPa) compared to the P(VDF-TrFE) film (0. 65 GPa). On the other hand, reinforcement with 20 wt% CFO, CZFO and NZFO fillers demonstrated a significant increase in the E_Y of the nanocomposite films to approximately 1 GPa. At the same time, NFM and FO particles only marginally improved Young's modulus compared to pure P(VDF-TrFE), exhibiting a value of approximately 0.8 GPa. The small agglomerations of CFO nanoparticles and the dimension of NdFeB microparticle into the composites may explain their slightly weaker mechanical performance. However, all films exhibited Young's modulus values in the same order of magnitude as those previously reported in polymer-based composites with high ME coupling [63]. The balance between stiffness and flexibility is essential for an optimized ME response [8]. The electrical coating had no significant influence on the mechanical properties of the composite (values with less than 2 % difference).

3.4. Piezoelectric, electric and dielectric properties

Fig. 4d displays the absolute value of the piezoelectric coefficient $|d_{33}|$ for the various composites. Measurements were conducted 2 days post-poling to minimize the electric charges accumulated during the polarization process. All d_{33} values are negative and in the following the modulus will be provided. The findings indicate that neat P(VDF-TrFE) and CFO5 films exhibit similar piezoelectric constants (20–22 $pC{\cdot}N^{-1}$), representing the highest values among all films, while NFM20 showed the lowest $|d_{33}|$ value of 9 $pC{\cdot}N^{-1}$. The remaining composites demonstrated intermediate $|d_{33}|$ values ranging from 11 to 19 $pC{\cdot}N^{-1}$. The observed reduction in piezoelectric response for composites with particle contents exceeding 5 wt% is attributed to a disruption in the piezoelectric matrix connectivity and interfacial mechanical imperfections. The decrease in the piezoelectric response of the NFM20 sample

can also be explained by the low crystallinity of the sample [63,64].

Electrical conductivity and dielectric characteristics (Fig. 5a) ensure effective electrical polarization under applied magnetic fields. Appropriate surface conductivity (without the electrode) and dielectric constant values are essential to facilitate the CME effect, where an electric field induces a change in sample's magnetization. The current-voltage (IV) curves (Fig. 5a) illustrate that all films exhibited Ohmic behaviour, characterized by a linear increase in current as the voltage increased. Notably, the incorporation of 20 % CFO and NZFO magnetic particles resulted in an enhancement of DC surface conductivity, reaching values between 4.26×10^{-10} and 2.2×10^{-10} S·m^{-1}, compared to 4.70×10^{-12} S·m^{-1} for pure P(VDF-TrFE). Despite this increase, none of the composites achieved conductivities below 10^{-3} S·m^{-3}, vital for a strong ME effect [8].

Regarding dielectric characteristics (Fig. 5c–d), the real component of the dielectric permittivity (ε′) diminished as frequency increased, attributed to dipole relaxation and crystalline/amorphous interface effects. Moreover, both ε′ and dielectric losses (tanδ) were observed to rise with the addition of magnetic particles. Two factors can explain this: firstly, the magnetic particles enhance polarization at their interface with P(VDF-TrFE), resulting in a higher dielectric constant; secondly, they also boost electrical conductivity, leading to increased dielectric losses [65,66].

Nevertheless, all films maintained tanδ values under 0.2, a crucial requirement for effective ME coupling [8].

The enhancement in dielectric properties and the consistency of dielectric losses post-electrical poling in the composites can be attributed to several key factors related to dipole alignment, crystallinity, and the interaction between the polymer matrix and magnetic fillers [66]. The improved dipole alignment can inhibit charge carrier movement and reduce relaxation processes, thus maintaining low dielectric losses. These piezoelectric and dielectric trends directly influence the ME coupling efficiency, but the filler-specific magneto-mechanical and interfacial properties also play a critical role, as discussed below. Furthermore, poling may optimize the interface between the polymer and the magnetic nanoparticles, ensuring that the nanoparticles positively contribute to the dielectric properties without introducing excessive energy dissipation [67].

3.5. Magnetoelectric properties

The DME properties of the compounds at room temperature were assessed using the Lock-in MFLI Zurich Instruments. To ensure reliability of the results, five replicates of each sample were performed (Fig. 6a–b).

Fig. 6a shows the initial frequency sweep to determine the resonance frequency of the samples. NFM20 presents the lowest resonance frequency value, at 10.98 kHz. On the other hand, CFO5 and CFO10 exhibited the highest values, approximately 16 kHz. All other samples present values between 12,7 kHz and 14.03 kHz.

Fig. 6b, referring to the electric field produced by the samples due to the DME effect, basically presents 3 groups of samples. The one with the highest voltage value is the CFO20, with 6.3×10^{-3} V and NZFO20 shows the lowest value, with approximately 9467×10^{-4} V. The other values are in the range between 1.59×10^{-3} V and 4.664×10^{-3} V.

The direct ME coefficient (α) value is calculated according to Eq. (6) for an effective comparison among samples Fig. 6c–d. The gradual increase in concentration is reflected in the linear increase in the α value for the CFO samples (5, 10 and 20 wt%). The lowest value is observed for CFO5 with 3.33×10^{2} mV·cm^{-1}·Oe^{-1}, followed by CFO10 with 4,05 ×

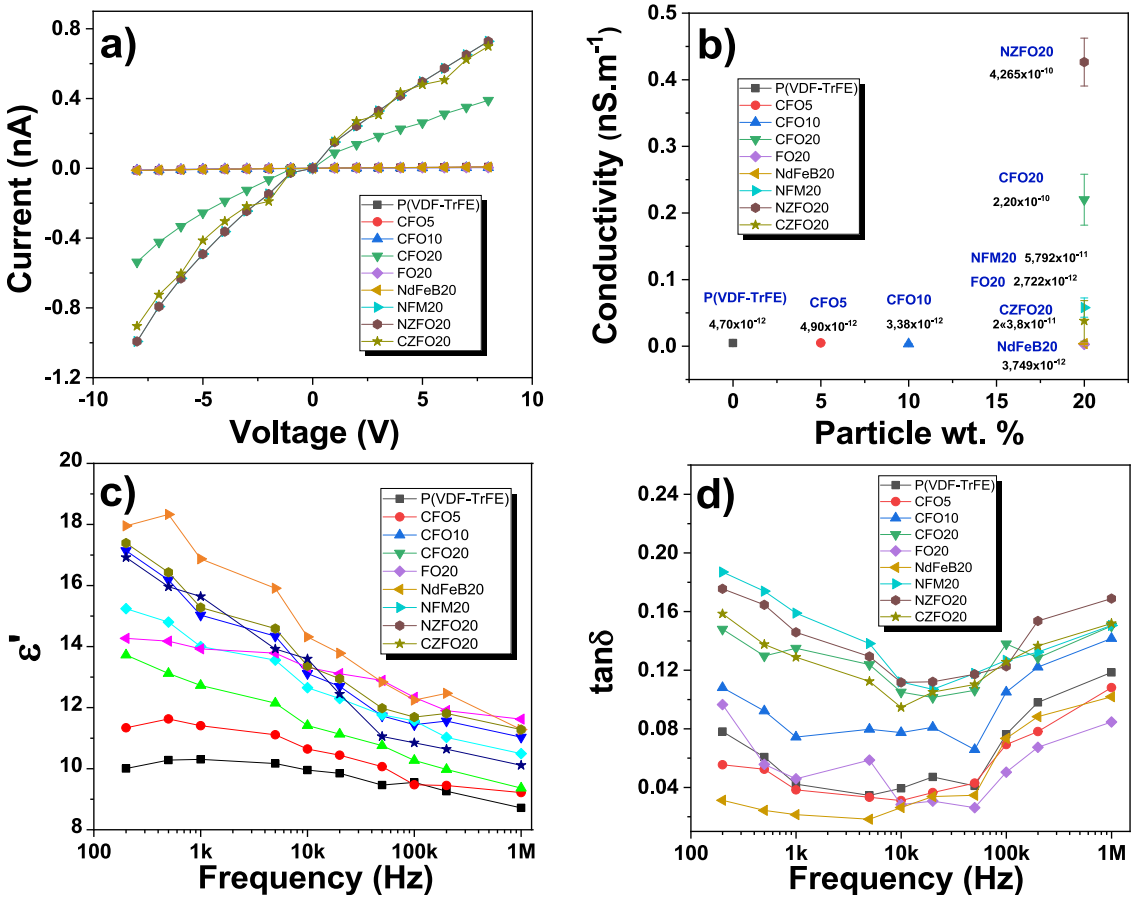

Fig. 5. a) Electric current variation as a function of applied voltage for the different samples. b) Electric conductivity values for each sample. c) Real part of the dielectric response and d) tanδ as a function of frequency for P(VDF-TrFE)-based composites with different filler type and content.

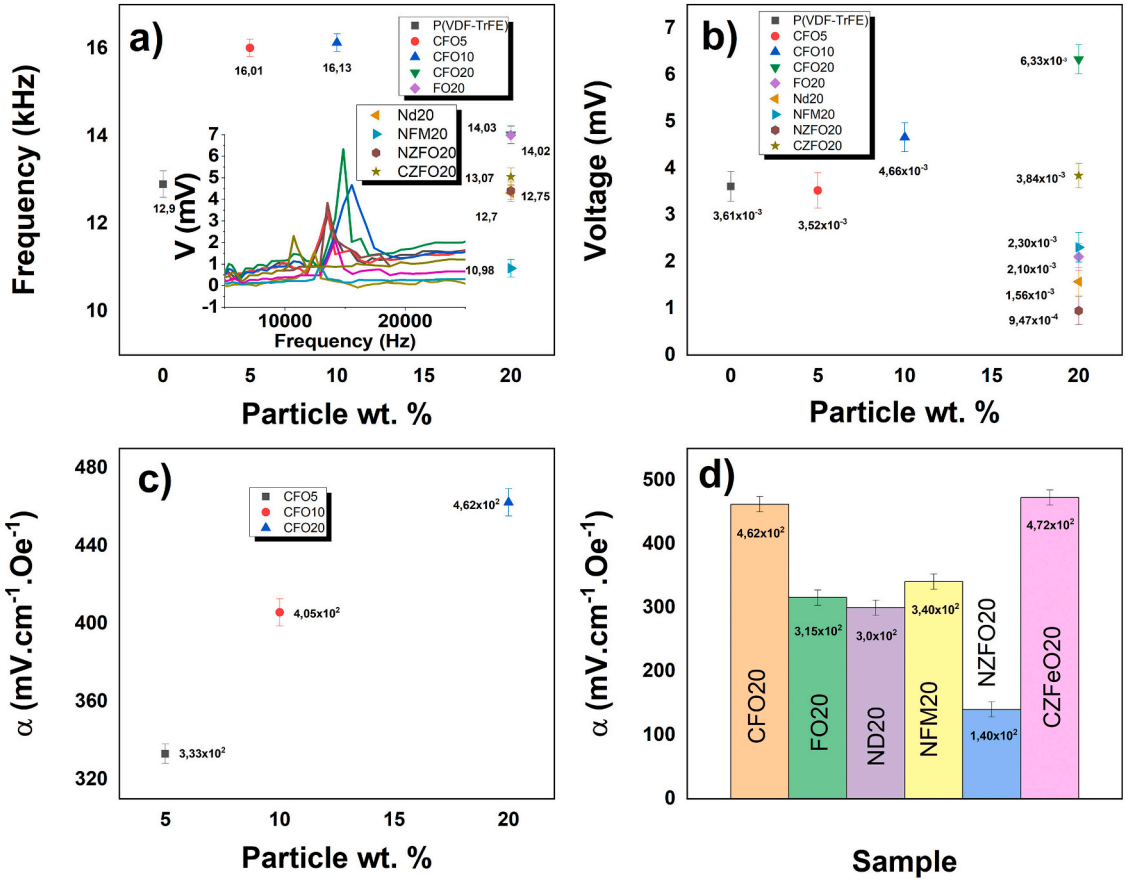

Fig. 6. Direct ME measurements. a) Frequency dependence of the direct ME response (V vs. f) for representative samples, with resonance peaks highlighted in the inset. Main plot shows the extracted resonance frequency as a function of magnetic particle type and weight percentage. b) Generated voltage for each sample. c) α for CFO5, 10 and 20 wt%. d) α for the different samples with 20 wt% filler.

10^2 mV·cm^{-1}·Oe^{-1}, the highest α value being shown by the CFO20 sample, with 4.62 × 10^2 mV·cm^{-1}·Oe^{-1}. This increase can be attributed to the rise in the overall magnetostriction due to the increase of the magnetostrictive phase within the ME composite [8,68].

The effect of filler type is obtained by comparing all composites with 20 % filler content, as presented in Fig. 6d. The lowest α value is found for the NZFO20 sample with 1,40 × 10^2 mV·cm^{-1}·Oe^{-1}; on the other hand, higher α values occur for CFO20 and CZFO20 samples with 4,62 × 10^2 and 4,72 × 10^2 mV·cm^{-1}·Oe^{-1} respectively. The remaining samples present values between 3,0 × 10^2 and 340 × 10^2 mV·cm^{-1}·Oe^{-1}.

The CME response of the different materials is presented in Fig. 7a–b.

Fig. 7a shows the initial frequency sweep to determine the resonance frequency of the different samples. CFO20 presents the highest recorded frequency value, at 16 kHz. The lowest value is for FO20, with approximately 10.4 kHz. All the other samples present values between 12,15 kHz and 13.97 kHz.

Fig. 7b, presents three different groups of samples, referring to the magnetic field produced by the samples. The highest magnetic field value is the CZFO20 with 33,94 Oe, CFO5 shows the lowest value with approximately 17,63 Oe. The other composites present magnetic field values ranging from 19,86 to 28,69 Oe.

Regarding that, the converse ME coefficient (α′) value was calculated according to Eq. (7) for all samples, as presented in Fig. 7c–d. The gradual increase in concentration leads to a linear increase n the converse alpha value for the CFO composite samples with 5, 10 and 20 wt% filler concentration. The lowest value is observed for CFO5 with 6176 mOe·cm·V^{-1}, followed by CFO10 with 7708 mOe·cm·V^{-1}. The highest α value resides in CFO20 with 9.003 mOe·cm·V^{-1}. This increase is attributed to the rise in the magnetostriction due to the increase of the magnetostrictive phase on the ME composite [8,68].

By comparing the results for the different fillers with 20 wt% filler content, Fig. 7d, the differences among samples is notable. The lowest α′ value occurs for the NZFO20 sample with 5.828 mOe·cm·V^{-1}. On the other hand, higher α′ values are observed for samples CFO20 and CZFO20 with 9.003 and 9.642 mOe·cm·V^{-1}, respectively. The remaining samples present α′ values between 6.72 and 8.014 mOe·cm·V^{-1}.

The differences observed in the ME response among the various composites can be attributed to several key physical parameters of the magnetostrictive fillers. First, the intrinsic magnetostrictive coefficient (λ) plays a dominant role: materials such as $CoFe_2O_4$ (−250 ppm) and $Co_{0.5}Zn_{0.5}Fe_2O_4$ (10 ppm) generate larger mechanical strains under a magnetic field, thereby inducing stronger electrical polarization via the piezoelectric matrix. Second, particle size and morphology directly influence filler dispersion and interfacial stress transfer. Nanometric fillers like $CoFe_2O_4$ (~35–50 nm) promote better mechanical coupling with the polymer matrix compared to micron-sized $Nd_2Fe_{14}B$ (~5 μm), which may introduce inhomogeneous strain distribution. Third, the electrical resistivity of the fillers affects the efficiency of dynamic ME coupling, with Zn-doped ferrites such as CZFO and NZFO exhibiting higher resistivity and reduced eddy current losses, thus improving ME signal fidelity. Lastly, the mechanical compatibility and interfacial adhesion between the fillers and the P(VDF-TrFE) matrix influence the strain transfer efficiency and the preservation of the piezoelectric phase, both critical for achieving optimal ME performance. These combined factors explain the material-dependent behaviour observed and confirm that rational filler selection is essential for maximizing ME coupling in flexible composite architectures.

Fig. 8a–b shows the variation of the resonance frequency as a

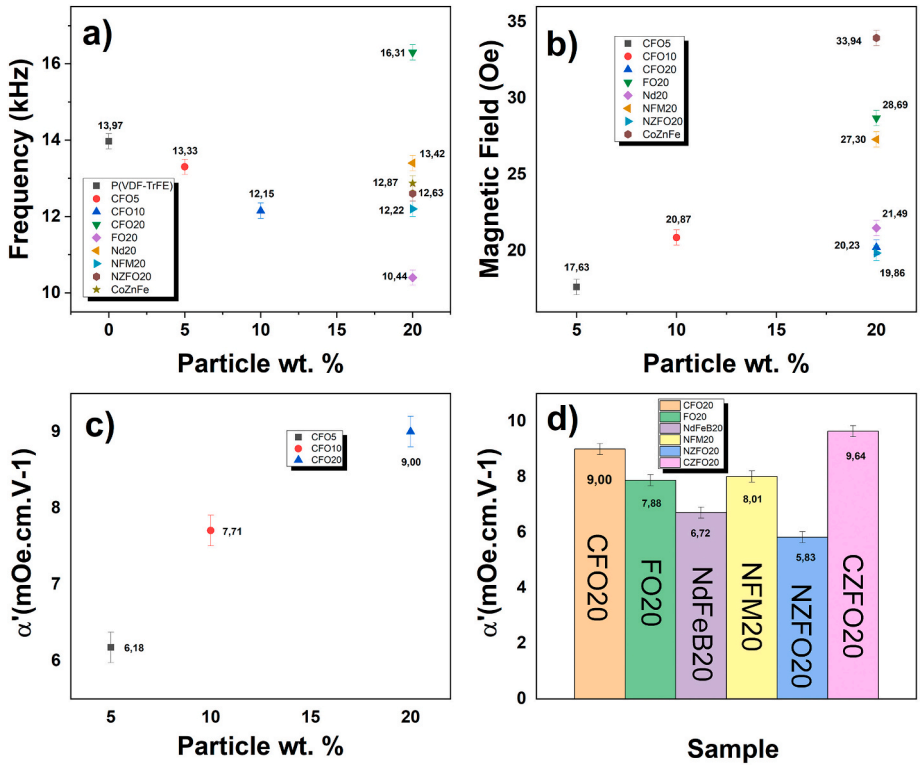

Fig. 7. Converse magnetoelectric measurements. a) Resonance frequency as a function of magnetic particle type and % by weight. b) Generated magnetic field for each sample. c) α' for CFO5, 10 and 20 % by weight. d) α' for the different samples with 20 % by weight.

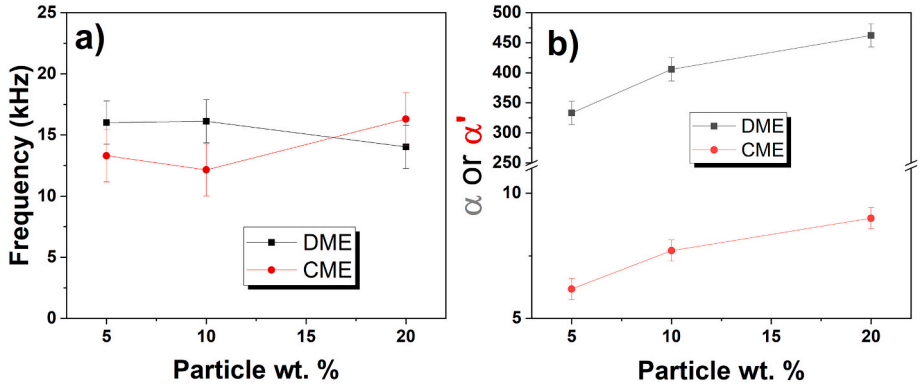

Fig. 8. Comparison of CFO samples with different particle wt% relative to DME and CME. a) As a function of the resonance frequency. b) as a function of ME coefficient.

Table 4
Converse ME coefficients (α') reported in the literature and their piezoelectric & magnetostrictive components as well as electrodes.

Type	Piezo element	Magneto element	H_i (Oe)	α' (mOe·cm.V^{-1})	Electrodes	Reference
2–2	Pb(*Zr*,*Ti*)O_3	Metglas	10	2750	Screen-printed	[69]
	PVDF	FeBSiC	–	90	Magnetron-sputtered	[70]
0–3	P(VDF-TrFE)	CFO#	8.1	6.29	Conventional vacuum-evaporated	[8]
		FO#	7.7	4.48		
		NdFeB#	7.3	4.41		
		NZFO#	19.9	5.83		
		NdFeB*,#	21.5	6.72		
		FO#	28.69	7.88	PulseForge-printed	This work
		NFM#	27.30	8.01		
		CFO#	20.23	9.00		
		CZFO#	33.94	9.64		

*micro-sized; #composite with 20 wt% of magnetostrictive filler.

function of the particle weight percentage for both DME and CME effects, showing a similar behaviour, with a progressive increase in resonance frequency with an increase in particle weight percentage up to 20 %, with values between 11 and 16 kHz.

Both values of α and α′ shows the same increase as a function of particle content. For DME, it reaches a maximum for the 20 % filler content sample, with around 472 $mV{\cdot}cm^{-1}{\cdot}Oe^{-1}$, while for the CME, the maximum is also reached for CFO20 with 9 $mOe{\cdot}cm{\cdot}V^{-1}$. These results present the same order of magnitude as those obtained previously in the literature.

To better compare all the results obtained, Table 4 presents a comparison with the literature.

Compared to the previously reported results using vacuum-evaporated electrodes [8], the use of PulseForge-printed thick electrodes leads to a marked enhancement in both H_i and α′ across all tested fillers. For the $CoFe_2O_4$-based composites, the generated magnetic field increases from 8.1 Oe to 20.2 Oe (a 149 % enhancement), while the α′ rises from 6.29 to 9.00 $mOe{\cdot}cm{\cdot}V^{-1}$, representing a 43 % increase. In the case of Fe_3O_4-based composites, the magnetic field increases from 7.7 Oe to 28.7 Oe, resulting in a 273 % improvement, and the α′ improves from 4.48 to 7.88 $mOe{\cdot}cm{\cdot}V^{-1}$ (76 % increase). For NdFeB-based composites, the magnetic field increases from 7.3 Oe to 21.5 Oe, reflecting a 195 % increase, and the α′ improves from 4.41 to 6.72 $mOe{\cdot}cm{\cdot}V^{-1}$, a 52 % enhancement. These substantial gains confirm that printed thick electrodes not only facilitate improved charge distribution and interfacial coupling but also act as a highly effective strategy to boost magnetoelectric performance in a scalable and energy-efficient manner.

The observed improvements in the generated magnetic field and α′ values for samples with printed electrodes suggest that electrode structuring significantly influences ME coupling: the introduction of thicker electrodes optimizes charge distribution and interfacial coupling, thereby enhancing the overall ME efficiency of the composite. This empirical evidence reinforces the idea that material structuring plays a decisive role in governing magnetic interactions, a concept that can be traced back to De Magnete, where William Gilbert laid the groundwork for understanding how structured magnetic bodies influence surrounding fields. In the same spirit, our findings demonstrate that adding a thicker electrode fundamentally alters the system's magnetoelectric response, optimizing its efficiency for spintronic applications.

In addition to demonstrating high ME coefficients, the CZFO20 sample generated a magnetic field of 33.94 Oe under an electric field of 400 $kV{\cdot}m^{-1}$, with power consumption in the nanowatt range due to the high resistivity of the composite and the low current required. Compared to conventional electromagnets, which typically consume 100–500 mW to generate comparable fields, this represents a power reduction of ~6 orders of magnitude. These values are compatible with previous reports on energy-efficient ME and voltage-driven spintronic systems that demonstrate switching energies in the sub-attojoule to attojoule range. This result highlights the strong potential of ME composites with printed electrodes for enabling ultra-low-power spintronic platforms [71–74].

4. Conclusions

This work demonstrates that engineering the geometry of printed electrodes in flexible magnetoelectric (ME) composites enables precise tuning of ME coupling, leading to significant improvements in functional performance. By optimizing electrode thickness using scalable fabrication techniques, namely Aerosol Jet Printing and photonic sintering, we achieved a 270 % increase in generated magnetic field (up to 34 Oe) and an 80 % enhancement in the converse ME coefficient, exceeding 9 $mOe{\cdot}cm{\cdot}V^{-1}$. These values surpass the minimum electric-field threshold required for spin manipulation by more than two orders of magnitude, positioning this strategy as a viable route for low-power spintronic applications.

Printed electrodes, approximately 300 times thicker than conventional vacuum-deposited ones, enable uniform charge distribution and enhanced interfacial coupling, without compromising the mechanical or piezoelectric integrity of the composite. This approach overcomes the thermal and mechanical limitations of traditional deposition methods and allows integration into flexible and scalable device architectures.

In particular, the CZFO20 sample generated a magnetic field of nearly 34 Oe under an electric field of 400 $kV{\cdot}m^{-1}$ with nanowatt-level power consumption, representing a power reduction of ~ 6 orders of magnitude compared to conventional current-driven field sources. Furthermore, their compatibility with additive manufacturing, through solution-based processing and direct deposition via printing techniques, enables seamless integration into spintronic devices such as spin valves.

This scalable approach bridges foundational physical concepts from *De Magnete* with modern engineering practices, offering a promising pathway for the development of tunable, high-performance ME devices.

Ultimately, this work establishes printed electrode design as a powerful, energy-efficient strategy for magnetic field generation in ME composites, paving the way toward sustainable, low-power spintronic technologies for data storage, logic circuits, and advanced sensing platforms.

CRediT authorship contribution statement

R. Carvalho: Writing – original draft, Visualization, Software, Resources, Methodology, Investigation. **L. Amorim:** Writing – original draft, Visualization, Validation, Software, Resources, Methodology, Investigation, Formal analysis. **C. Ribeiro:** Writing – original draft, Visualization, Validation, Software, Resources, Project administration, Methodology, Investigation, Funding acquisition. **S. Lanceros-Mendez:** Writing – review & editing, Visualization, Validation, Supervision, Project administration, Funding acquisition. **M. Serpelloni:** Writing – review & editing, Project administration, Methodology, Investigation, Conceptualization. **G. Polidori:** Writing – review & editing, Resources, Project administration, Methodology, Investigation. **P. Martins:** Writing – review & editing, Writing – original draft, Visualization, Validation, Supervision, Resources, Project administration, Methodology, Funding acquisition, Conceptualization.

Declaration of competing interest

The authors declare that they have no known competing financial interests or personal relationships that could have appeared to influence the work reported in this paper.

Acknowledgments

The authors express their gratitude to FCT (Fundação para a Ciência e Tecnologia) for financial support within the framework of Strategic Funding UID/04650/Centro de Física das Universidades do Minho e do Porto (2025-2029) and under project 2022.05540.PTDC (https://doi.org/10.54499/2022.05540.PTDC). RC acknowledges support from FCT under grants 2022.13206.BD (https://doi.org/10.54499/2022.13206.BD). This study forms part of the Advanced Materials program and was supported by MCIN with funding from European Union NextGenerationEU (PRTR-C17.I1) and by the Basque Government under the IKUR program. Funding from the Basque Government Industry Department under the ELKARTEK program is also acknowledged.

Data availability

Data will be made available on request.

References

[1] W. Gilbert, De Magnete, Courier Corporation, 2013.

[2] N. Kipnis, Chance in Science: the discovery of Electromagnetism by HC Oersted, Sci. & Educ. 14 (1) (2005) 1–28.
[3] R.D.A. Martins, Resistance to the discovery of electromagnetism: Ørsted and the symmetry of the magnetic field, in: Volta and the History of Electricity, 2003, pp. 245–266.
[4] S. Chatterjee, Michael Faraday: discovery of electromagnetic induction, Resonance 7 (3) (2002) 35–45.
[5] J.C. Maxwell, The Scientific Letters and Papers of James Clerk Maxwell Vol. 1, CUP Archive, 1990, pp. 1846–1862.
[6] L. Dong, et al., Integration of photo/magnetic responsive composite phase change materials with polyurethane sponge for sustainable and efficient cleanup of crude oil spills, Chem. Eng. J. 496 (2024).
[7] S. Wang, et al., Design of CuS composite carbon-based Ni Al-LDH multifunctional phase change composite with electromagnetic shielding performance and heat storage capacity, Chem. Eng. J. 491 (2024).
[8] R. Carvalho, S. Lanceros-Mendez, P. Martins, Tailoring polymer-based magnetoelectrics for spintronics: evaluating the converse effect, Appl. Mater. Today 38 (2024) 102216.
[9] P. Martins, et al., Magnetoelectrics for biomedical applications: 130 years later, bridging materials, energy, and lifeWriting, Nano Energy 126 (2024).
[10] D.C. Kakarla, et al., Exploring new members of magnetoelectric materials in CuO–CuCl2–SeO2 system, Mater. Today Phys. (2024) 46.
[11] R. Brito-Pereira, et al., From rare-earth hazardous waste to all-in-one sustainable energy, sensing, and actuation, Chem. Eng. J. 465 (2023).
[12] V.A. L'Vov, et al., Giant magnetoelectric effect of Ni–Mn-Ga/piezopolymer composites tailored by a martensitic transformation, Compos. Sci. Technol. 241 (2023).
[13] R. Brito-Pereira, et al., Environmentally friendlier wireless energy power systems: The coil on a paper approach, Nano Energy 111 (2023).
[14] R. Brito-Pereira, et al., Printed multifunctional magnetically activated energy harvester with sensing capabilities, Nano Energy 94 (2022).
[15] P. Martins, et al., In a search for effective giant magnetoelectric coupling: magnetically induced elastic resonance in Ni-Mn-Ga/P (VDF-TrFE) composites, Appl. Mater. Today 29 (2022) 101682.
[16] P. Martins, S. Lanceros-Méndez, Polymer-based magnetoelectric materials: to be or not to be, Appl. Mater. Today 15 (2019) 558–561.
[17] X. Sun, et al., Progressive hollow engineering induced raspberry-like magnetoelectric microspheres via synergistic etching-assembly strategy toward boosted microwave attenuation, Chem. Eng. J. 499 (2024).
[18] P. Martins, et al., Spray-Printed Magnetoelectric Multifunctional Composites. Composites Part B: Engineering, 2020, p. 187.
[19] A.C. Lima, et al., All-printed multilayer materials with improved magnetoelectric response, J. Mater. Chem. C 7 (18) (2019) 5394–5400.
[20] T. Jing, et al., Magnetostriction enhanced self-powered nanofiber sheet as cardiac patch with magnetoelectric synergistic effect on actuating Na+ k+-ATPase, Chem. Eng. J. 490 (2024).
[21] Z. Cheng, et al., 3D printed composites based on the magnetoelectric coupling of Fe/FeCo@C with multiple heterogeneous interfaces for enhanced microwave absorption, Chem. Eng. J. 480 (2024).
[22] G. Fang, et al., Determining the preferable polarization loss for magnetoelectric microwave absorbers by strategy of controllably regulating defects, Chem. Eng. J. 463 (2023).
[23] P.M. Martins, et al., Magnetic nanoparticles for biomedical applications: from the soul of the Earth to the deep history of ourselves, ACS Appl. Bio Mater. 4 (8) (2021) 5839–5870.
[24] N. Pereira, et al., Magnetoelectrics: Three centuries of research heading towards the 4.0 industrial revolution, Materials 13 (18) (2020).
[25] P. Martins, et al., Advances in printing and electronics: from engagement to commitment, Adv. Funct. Mater. 33 (16) (2023).
[26] R. Carvalho, et al., Energy-efficient electric control of magnetization in polymer-based magnetoelectrics for spintronic applications, Commun. Mater. 6 (1) (2025).
[27] J. Gao, et al., Review of magnetoelectric sensors, in: Actuators, MDPI, 2021.
[28] L. Herrera Diez, et al., Magnetoelectric materials, phenomena, and devices, APL Mater. 9 (5) (2021).
[29] X. Liang, H. Chen, N.X. Sun, Magnetoelectric materials and devices, in: APL Materials 9, 2021, p. 4.
[30] X. Liang, et al., Roadmap on magnetoelectric materials and devices, IEEE Trans. Magn. 57 (8) (2021) 1–57.
[31] Z. Chu, M. PourhosseiniAsl, S. Dong, Review of multi-layered magnetoelectric composite materials and devices applications, J. Phys. D Appl. Phys. 51 (24) (2018) 243001.
[32] Z.B. Muche, et al., Integrating electrodes and PVDF-HFP/Kevlar nanofiber separator for multi-functions using electrospinning, Chem. Eng. J. 505 (2025).
[33] X. Sun, et al., Reducing equivalent magnetic noise by electrode design and magnetic annealing in Quartz/Metglas magnetoelectric sensors, Sens. Actuators A Phys. 379 (2024) 115903.
[34] C.M. Leung, et al., Advancing eddy current detection probes with magnetoelectric composite Materials: Enhancing crack detection in conductive materials, J. Magn. Magn. Mater. 592 (2024) 171816.
[35] X. Pan, et al., Research progress of high-performance micron-sized electrode materials for supercapacitors with a promising future, J. Energy Storage 108 (2025) 115177.
[36] Y. Cheng, et al., Recent development and status of magnetoelectric materials and devices, Phys. Lett. A 382 (41) (2018) 3018–3025.
[37] D. Cao, et al., Role of electrodes materials in determining the interfacial and magnetoelectric properties in BaTiO 3-based multiferroic tunnel junctions, Eur. Phys. J. B 90 (2017) 1–6.
[38] S. Fabiano, et al., Ferroelectric polarization induces electronic nonlinearity in ion-doped conducting polymers, Sci. Adv. 3 (6) (2017).
[39] Y. Ahn, J.Y. Son, Enhanced ferroelectric properties of P(VDF-TrFE) thin films from Nb nanopin electrodes, Polymer 180 (2019).
[40] S. Xu, et al., Magnetoelectric coupling in multiferroics probed by optical second harmonic generation, Nature Commun. 14 (1) (2023).
[41] C. Johannes, et al., The influence of thermal and mechanical stress on the electrical conductivity of ITO-coated polycarbonate films, Polymers 15 (11) (2023).
[42] P. Jayaraman, et al., Boosted ion switching at the electrode-electrolyte interfaces of architecture interdigitated flexible supercapacitors, Mater. Today Phys. (2025) 51.
[43] Y. Niu, et al., Ultrathin MXene/Ag-Ag nanocomposite films for 3D-conformal electromagnetic shielding via aerosol jet printing, Chem. Eng. J. 506 (2025).
[44] T.Y. Choi, et al., Directly patterned ITO nanoparticle-based transparent electrode using co-solvent-based aerosol jet printing for transparent thin film heaters, Chem. Eng. J. 498 (2024).
[45] S.P. Sreenilayam, et al., Additive-free silver nanoparticle ink development using flow-based Laser Ablation Synthesis in Solution and Aerosol Jet printing, Chem. Eng. J. 449 (2022).
[46] J. Krzeminski, et al., Photonic curing of silver paths on 3D printed polymer substrate, Circuit World 45 (1) (2019) 9–14.
[47] P. Martins, M. Silva, S. Lanceros-Mendez, Determination of the magnetostrictive response of nanoparticles via magnetoelectric measurements, Nanoscale 7 (21) (2015) 9457–9461.
[48] A.E. Clark, et al., Magnetostrictive properties of Galfenol alloys under compressive stress, Mater. Trans. 43 (5) (2002) 881–886.
[49] M. Atif, et al., Studies on the magnetic, magnetostrictive and electrical properties of sol-gel synthesized Zn doped nickel ferrite, J. Alloys Compd. 509 (18) (2011) 5720–5724.
[50] H. He, Synthesis and magnetic properties of Co0. 5Zn0. 5Fe2O4 nanoparticles by template-assisted combustion method, Mater. Manuf. Process. 27 (9) (2012) 901–904.
[51] M. Staruch, et al., Structural and magnetic properties of CoFe2O4 and Co0.5Zn0.5Fe2O4 nanoparticles for the magnetoelectric composite films, Integr. Ferroelectr. 131 (1) (2011) 102–109.
[52] P. Martins, A.C. Lopes, S. Lanceros-Mendez, Electroactive phases of poly (vinylidene fluoride): determination, processing and applications, Prog. Polym. Sci. 39 (4) (2014) 683–706.
[53] C. Cao, et al., Ultra-sensitive flexible piezoelectric sensor based on P(VDF-TrFE) films with integrated fillers encased in organic conductive shells, Chem. Eng. J. 509 (2025).
[54] Y. Ra, et al., Direct electrospinning of reconstructable PVDF-TrFE nanofibrous mat onto conductive cement nanocomposite for triboelectricity-assisted net zero energy structure, Chem. Eng. J. 485 (2024).
[55] T. Siponkoski, et al., A printable P (VDF-TrFE)-PZT composite with very high piezoelectric coefficient, Appl. Mater. Today 20 (2020) 100696.
[56] N. Jia, et al., Crystallization behavior and electroactive properties of PVDF, P(VDF-TrFE) and their blend films, Polym. Test. 57 (2017) 302–306.
[57] D.D. Tang, Y.-J. Lee, Magnetic Memory: Fundamentals and Technology, Cambridge University Press, Cambridge, 2010.
[58] Y. Mao, Q. Jiao, Y. Shi, Performance optimization for magnetoelectric antennas based on a multi-field coupling analysis model, J. Appl. Phys. 136 (11) (2024).
[59] P. Martins, C.M. Costa, S. Lanceros-Mendez, Nucleation of electroactive β-phase poly (vinilidene fluoride) with CoFe 2 O 4 and NiFe 2 O 4 nanofillers: a new method for the preparation of multiferroic nanocomposites, Appl. Phys. A 103 (2011) 233–237.
[60] R. Gonçalves, et al., Nucleation of the electroactive β-phase, dielectric and magnetic response of poly (vinylidene fluoride) composites with Fe2O3 nanoparticles, J. Non Cryst. Solids 361 (2013) 93–99.
[61] T.C. Chung, A. Petchsuk, Synthesis and properties of ferroelectric fluoroterpolymers with curie transition at ambient temperature, Macromolecules 35 (20) (2002) 7678–7684.
[62] H. Su, A. Strachan, W.A. Goddard Iii, Density functional theory and molecular dynamics studies of the energetics and kinetics of electroactive polymers: PVDF and P(VDF-TrFE), Phys. Rev. B Condens. Matter. Mater. Phys. 70 (6) (2004) 064101.
[63] A.C. Lima, et al., Greener solvent-based processing of magnetoelectric nanocomposites, ACS Sustain. Chem. Eng. 10 (13) (2022) 4122–4132.
[64] R. Brito-Pereira, et al., Magnetoelectric response on Terfenol-D/ P(VDF-TrFE) two-phase composites, Compos. Part B Eng. 120 (2017) 97–102.
[65] R. Gonçalves, et al., Nucleation of the electroactive β-phase, dielectric and magnetic response of poly(vinylidene fluoride) composites with Fe2O3 nanoparticles, J. Non Cryst. Solids 361 (2013) 93–99.
[66] M.S. Sebastian, et al., Understanding nucleation of the electroactive β-phase of poly (vinylidene fluoride) by nanostructures, RSC Adv. 6 (114) (2016) 113007–113015.
[67] G. Liu, et al., Losses in ferroelectric materials, Mater. Sci. Eng. R: Reports 89 (2015) 1–48.
[68] P. Martins, et al., Wide-range magnetoelectric response on hybrid polymer composites based on filler type and content, Polymers 9 (2) (2017) 62.
[69] Y. Zhang, et al., Converse magnetoelectric effect in laminated composite of Metglas and Pb(Zr,Ti)O3 with screen-printed interdigitated electrodes, AIP Adv. 4 (6) (2014).

[70] L.Y. Fetisov, et al., Magnetoelectric direct and converse resonance effects in a flexible ferromagnetic-piezoelectric polymer structure, J. Magn. Magn. Mater. 485 (2019) 251–256.
[71] D.C. Ralph, Comment on "Spin-orbit logic with magnetoelectric nodes: a scalable charge mediated nonvolatile spintronic logic", Mesoscale Nanoscale Phys. (2016) 1–2, 1607.06690v1.
[72] S. Husain, Z. Yao, R. Ramesh, Enabling magnetoelectric spin-orbit logic and memory, Newton 1 (1) (2025).
[73] D.C. Vaz, et al., Voltage-based magnetization switching and reading in magnetoelectric spin-orbit nanodevices, Nat. Commun. 15 (1) (2024) 1902.
[74] B. Prasad, et al., Ultralow voltage manipulation of ferromagnetism, Adv. Mater. 32 (28) (2020) 2001943.